Analysis of the EMCCD point-source response using x-rays

I. V. Kotov[a,*], S. Hall[b], D. Gopinath[c], A. Barbour[a], J. Li[a], Y. Gu[a], K. Holland[c], A. Holland[d], I. Jarrige[a], J. Pelliciari[a], M. Soman[d], S. Wilkins[a], V. Bisogni[a]

[a] *Brookhaven National Laboratory, Upton, NY 11973, USA*
[b] *Physics, CUNY York College, Jamaica, NY 11451*
[c] *XCAM Ltd., Northampton, UK*
[d] *Centre for Electronic Imaging, The Open University, Milton Keynes, MK7 6AA, UK*

Abstract

Electron Multiplying Charge Coupled Devices, EMCCD are used as x-ray detectors. The NSLS-II Soft Inelastic x-ray Scattering (SIX) beam line has two EMCCDs for x-ray detection in the spectrometer arm. The spectrometer with high resolving power disperses x-rays vertically. The x-ray vertical position on the sensor plane is related to its energy. This allows for very accurate x-ray energy measurements through x-ray coordinates. X-rays interact with silicon and create a number of electron-hole pairs proportional to the x-ray energy. Electrons drift and diffuse toward pixel gates and are collected there. The diffused electrons form a charge cloud distributed over several neighboring pixels. This charge sharing enables coordinate measurements with accuracy better than the pixel pitch. The charge distribution shape has to be taken into account to achieve ultimate accuracy in coordinate measurements. In this paper, we present a method of the charge distribution shape analysis and demonstrate its applications.

The drift and diffusion of electrons from the point of generation to pixel gates results in the bell-shaped electron cloud usually approximated by Gaussian shape. The number of electrons collected under a pixel is proportional to the shape function integral. These electron packets get transferred to the sense node of the output amplifier. The transfer process could introduce distortions to the original charge distribution. For example, during transfers, electrons in the packet could be exposed to traps if they are present in the sensor. The trapping and later the release processes distort the apparent shape of the charge distribution. Therefore, deviations of the charge distribution shape from the originally symmetrical form can indicate the presence of trap centers in the sensor and can be used for sensor diagnostics.

Keywords: EMCCD, charge distribution shape, charge transfer efficiency, x-ray detectors

*Corresponding autor
Email address: kotov@bnl.gov (I. V. Kotov)

1. INTRODUCTION

The soft x-ray spectrometer on the SIX beam line [1] is equipped with e2v CCD207-40 [2] sensors. They are n-channel, partially depleted, back-illuminated devices with pixel size $16\mu m$. There is no AR coating on the back side to ensure a high efficiency for soft x-rays. The first $\sim 8\mu m$ at the back side is field-free. The total device thickness is $\sim 14\mu m$. The imaging area is $1632(columns) \times 1608(rows)$ pixels. In our case the direction of the parallel transfer (along columns) is close to the vertical and serial register is oriented in horizontal direction. The serial register has 536 electron multiplication elements. Sensors were operated at -110C. The readout speed was ~ 3 MHz.

The x-ray energy range available at this beam line is 0.23 keV – 2.0 keV. The x-ray absorption length in Silicon for these energies [3] is $0.1 - 10\mu m$. The conversion point for most of these x-rays is in the field-free region close to the entrance window surface. Initially the generated charge is contained in the volume constrained by the photo electron range in Silicon, $R[\mu m] = 0.012 * E[keV]^{1.75}$ [4]. For the maximum beam energy, R is $0.04\mu m$. The charge carriers diffuse in the field-free region and on the drift path. The resulting cloud shape is discussed, for example in [5], [6] and references therein. In our case the charge distribution width, σ is approximately $7 - 8\mu m$ at the EMCCD gates. The charge sharing between neighboring pixels enables charge cloud centroid determination for each individual x-ray. The approach based on center-of-mass method improves spatial resolution as demonstrated in [7] and references therein. Using the accurate charge distribution shape can lead to further resolution improvements.

2. Data and analysis

EMCCDs were calibrated at 285, 450, 530, 640, 760, 850, 930, 1050, 1200, 1409, 1500, 1750, and 2000 eV. The monochromatic x-ray beam was scattered off the target onto EMCCDs. To accumulate x-ray statistics, two hundred images with a short, $\sim 1sec$ integration time were taken at each energy. This results in ~ 100 x-rays per image. The short integration time was chosen to reduce pileup.

The following cuts were used in our analysis: a) pixels with amplitude greater than $10 \cdot \sigma_{noise}$ were considered as cluster seed candidates; b) all clusters with overlapping zones were rejected; c) clusters with total amplitude in the energy window centered on the beam energy were selected. The individual pixel and x-ray total amplitude distributions are shown in Fig.1 for 530 eV data. The peak at zero in pixel amplitude distribution corresponds to empty pixels and its width characterizes the readout noise.

The average x-ray cluster method presented in Ref.[8] is used for the charge distribution shape analysis. The x-ray cluster is defined as a $N \times N$ zone around the pixel with maximum amplitude. From a collection of clusters the average cluster is constructed. More details on average cluster shape and its variability are discussed in [8]. The average charge profile was augmented with the correlation matrix. Correlation coefficients between signal amplitudes in the central pixel and all other pixels in the cluster were calculated.

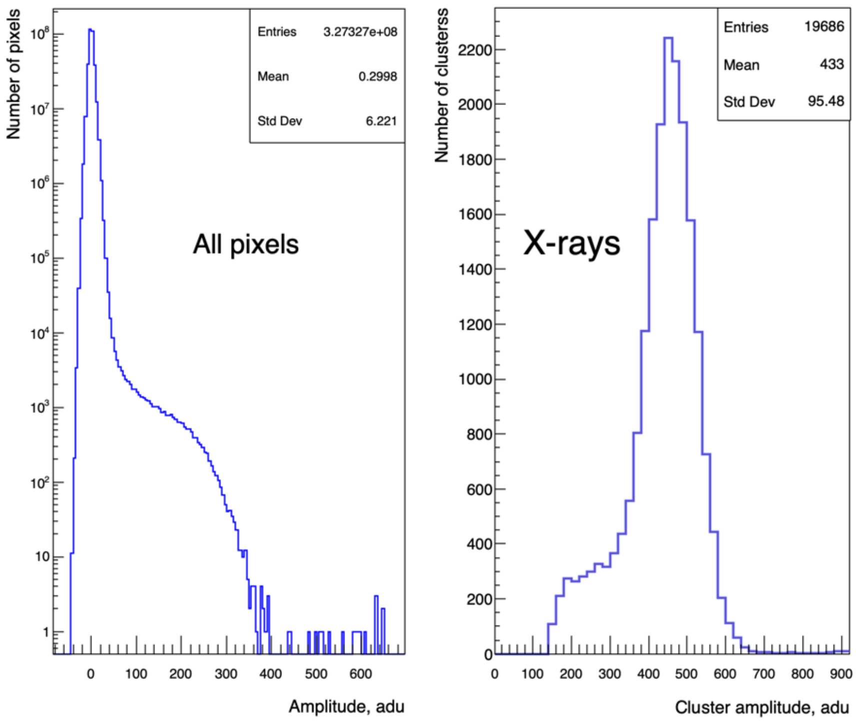

Figure 1: Pixel amplitudes and clean x-ray clusters total amplitudes at 530 eV.

Calibration data were analyzed using the 5x5 cluster size. Even though 3x3 zone contains most of the signal, the larger zone shows more charge distribution shape details; reduces the pileup contamination (compared to 3x3 zone); and the signal leakage out of this zone is much less as well. An array of histograms, an example is shown in Fig.2, is used to accumulate amplitude distributions in each cluster pixel and calculate averages and r.m.s. The 1D profiles in the serial and parallel transfer directions were also constructed. As an example, profile histograms obtained at 530 eV are shown in Fig.4 and Fig.5.

3. Average x-ray cluster shape

The number of non overlapping clusters in the 530 eV sample is $\sim 20k$. The number of rejected overlapping clusters is $\sim 3\%$. These numbers are typical for other energies as well. The average cluster 2D and 1D profiles are shown in Fig.4 and Fig.5. The average cluster is expected to be rotationally symmetrical around the central pixel. Our data clearly show an asymmetry in the horizontal direction at operating temperature -110C. One way to quantify this asymmetry is to calculate left-right and up-down differences as a total amplitude fraction for pixels close and away from the central pixel, numbered as 2: $e_1 = (A_3 - A_1)/A_{total}$ and $e_2 = (A_4 - A_0)/A_{total}$. These asymmetries are related to the charge transfer inefficiency. The e_1 characterizes the first pixel in the tail and e_2 is for the second pixel. The accuracy in asymmetry can be calculated

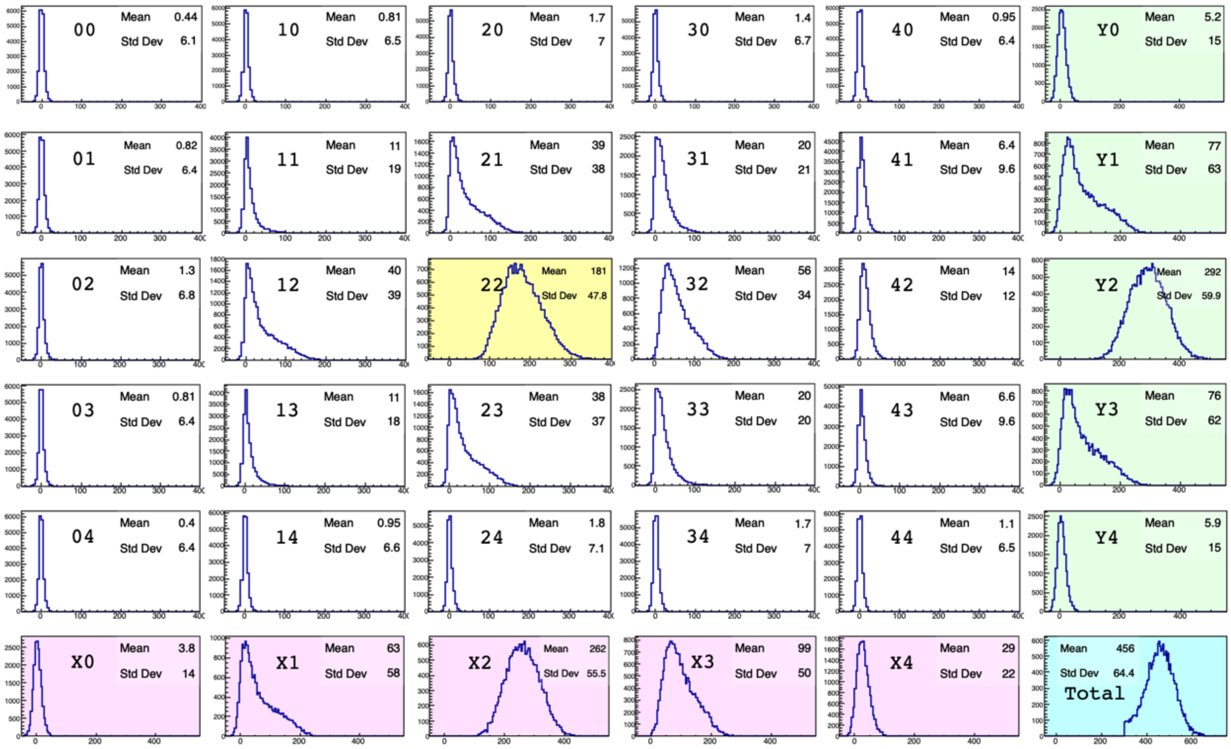

Figure 2: Amplitude distributions in 5×5 pixel clusters and horizontal and vertical profiles. The central pixel is highlighted in yellow; vertical profile is green; horizontal profile is pink; and total sum is blue. (For interpretation of the references to color in this figure legend, the reader is referred to the web version of this article.)

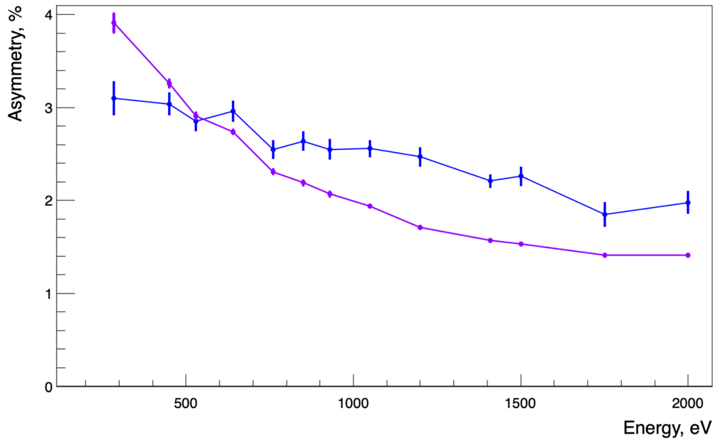

Figure 3: Average cluster central row asymmetry values for different x-ray energies. e_1 - blue, e_2 - magenta. Data points are connected by lines to guide the eye. (For interpretation of the references to color in this figure legend, the reader is referred to the web version of this article.)

using corresponding standard deviations. In our case the accuracy is $\Delta e \simeq 0.13\%$. The vertical profile top-bottom asymmetries are $e_1^V = 0.13\%$ and $e_2^V = 0.15\%$. They are within our measurement accuracy. The horizontal profile asymmetries are $e_1^H = 7.3\%$ and $e_2^H = 5.5\%$ as can be seen in Fig.5, left plot. All cluster rows contribute into asymmetry of the horizontal profile (sum over all cluster rows), as seen in Fig. 2, and there is a difference between central row and profile asymmetry values. Asymmetries slightly decrease with increasing energy. As an example, the energy dependence of the cluster central row asymmetry is shown in Fig.3 . The number of electrons in the charge packet increases with energy and since the number of traps stays constant this leads to the observed behavior. The asymmetry in the serial direction introduces systematic bias in this coordinate estimate. While it is true that the cluster vertical direction is the critical one since it directly impacts the energy resolution of RIXS experiments, a systematic bias in the horizontal charge profile may induce small deviations which are not ideal when the energy resolution is pushed to the limit. In our setup no provision was made in hardware for x-ray detector alignment in respect to the spectrometer coordinate system and isoenergetic lines of the RIXS spectrometer are not perfectly parallel to EMCCD rows. The alignment is done using calibration data sets. The coordinate along energy dispersion axis in the spectrometer system, y_s is related to detector coordinates $[x_d, y_d]$ by rotational transformation $y_s = y_d \cdot \cos(\alpha) + x_d \cdot \sin(\alpha)$ where α is the misalignment angle of two coordinate systems determined from calibration data. The uncertainty in x_d contributes into the energy resolution though suppressed by factor $\sin(\alpha)$. Furthermore, the asymmetry in the horizontal charge profile complicates a centroiding analysis based on center of mass or a 2D fitting, and requires an energy dependent correction to be established.

4. Correlation matrix

Pearson's correlation coefficients [9] between the central pixel and all other pixels in the cluster were calculated. X-rays in our sample are monochromatic and when the central pixel gets more signal other pixels get less. The charge distribution width and consequently the amplitude in the central pixel depends on the distance between the x-ray conversion point and the gates. These data features induce the negative correlation coefficients. The matrix is also expected to be centrally symmetrical for a non distorted charge distribution. For presentation purposes, the central pixel self correlation was set to zero instead of one. An example of the correlation matrix is shown in Fig.6. As seen in Fig.6 left plot the matrix is not entirely symmetrical. In the horizontal (serial) direction pixels in the tail have positive correlation coefficients, and left/right coefficients are -0.041, and $+0.075$. In the vertical direction corresponding coefficients, top/bottom are -0.04, and -0.046

5. Performance optimization

Analysis tools described in previous sections enable us to conduct the sensor performance optimization. The observed asymmetry in serial direction in both average cluster shape and correlation matrix suggested that one possible cause could be the multiplication part of the serial register. The presence of traps in the serial register could be the explanation. Taking into account the number of electron-multiplying stages, 536 the charge transfer inefficiency per stage is $\sim 5 \cdot 10^{-5}$.

The voltage settings on DC and HV multiplication register phases [10] directly affect the multiplication process and the path electrons follow during the transfer. The voltage difference between these phases sets the multiplication factor. For a given multiplication the parameter space is one dimensional. At the first optimization step we varied the DC phase voltage level. There were no changes in asymmetry parameters within 2σ level.

The EMCCD operating temperature strongly affect trapping and release time constants. On the next step we changed the operating temperature from nominal -110C to -95C in 5C increments. Measurements were always done at 532 eV. At each temperature point 120 images were acquired resulting in $\sim 40k$ x-rays per sensor. The average cluster 2D and horizontal profiles, and correlation matrices are shown in Fig.4, Fig.5 and Fig.6 correspondingly. The 2D and 1D profiles show that the tail disappears at warmer temperature. Asymmetry parameters are summarized in Table 1. The average cluster and correlation matrix symmetry is getting restored at warmer temperature. At -95C asymmetry parameter values are reduced by factor of ~ 20 and are within 3σ of parameter errors.

The operating temperature also strongly affects the multiplication gain and this in turn affects the system noise. The multiplication gain decreases at warmer temperatures, as expected, see [11], for example. The combined effect of all noise sources is reflected in the sensor energy resolution. Main noise sources are

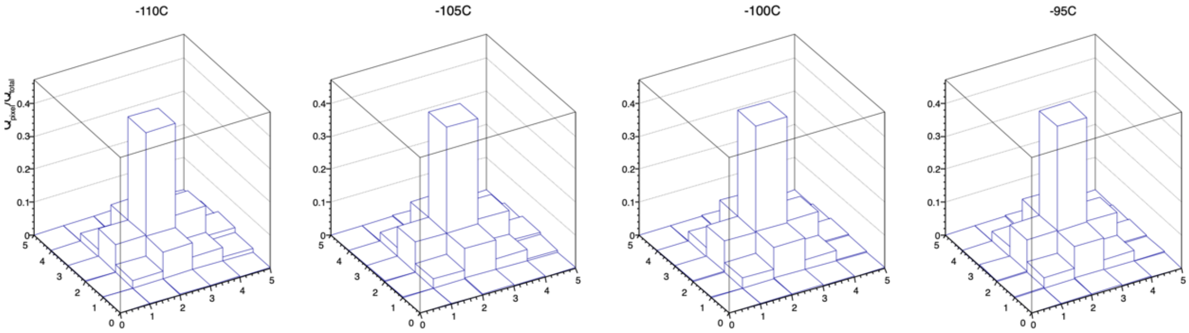

Figure 4: Average cluster at -110C, -105C, -100C, -95C.

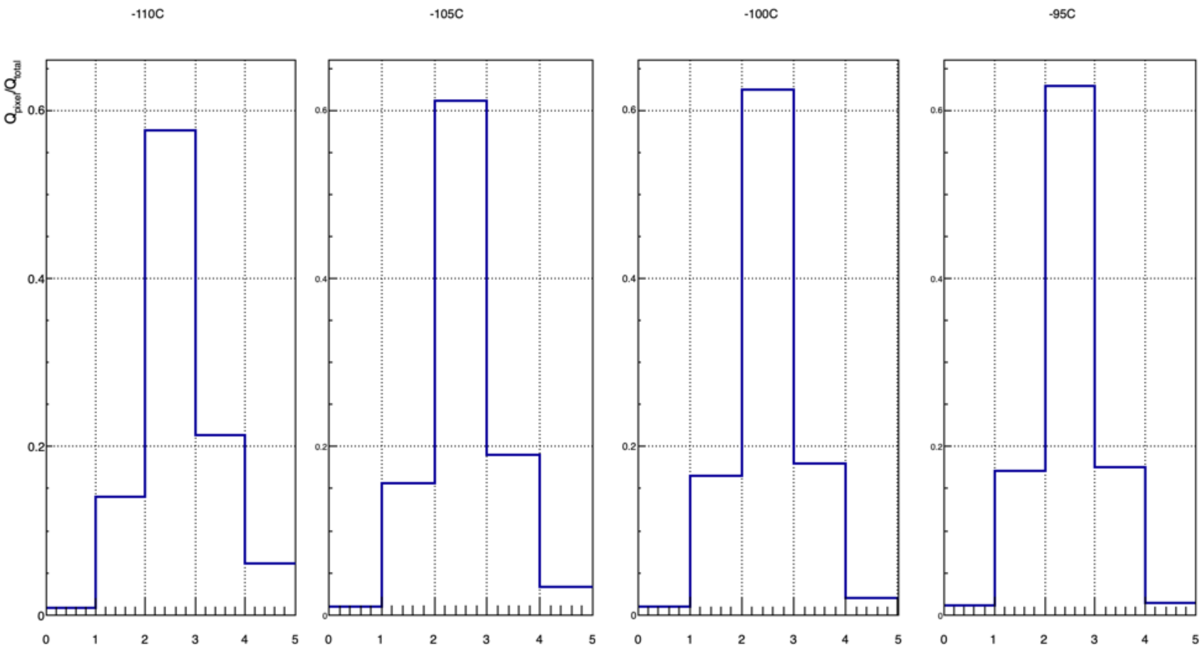

Figure 5: Horizontal (serial) profiles at -110C, -105C, -100C, -95C.

Table 1: Average cluster horizontal asymmetry.

T, C	e1, %	e2, %
-110	7.3	5.2
-105	3.3	2.3
-100	1.4	1.1
-95	0.36	0.39

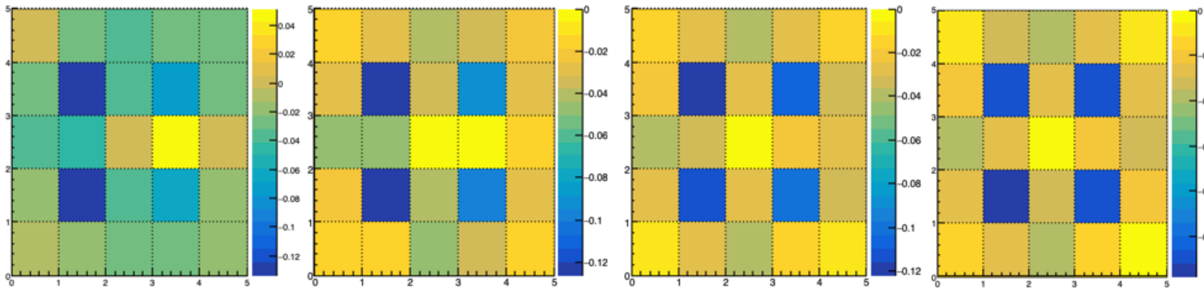

Figure 6: Correlation matrices for -110C, -105C, -100C, -95C (left to right). (For interpretation of the references to color in this figure legend, the reader is referred to the web version of this article.)

signal fluctuations, dark current, multiplication, readout and deferred charge. Fluctuations in the number of generated electron-hole pairs, signal shot noise σ_{signal} can be determined using the pair creation energy, w and the Fano factor, F. For our case E=532 eV, w = 3.72 eV/pair, F=0.14 [12] and the number of generated pairs is $N_e = E/w = 143$ and $\sigma_{signal} = \sqrt{F \cdot N_e} = 4.5e$. The electron multiplication contribution is usually expressed through the excess noise factor [13] $F_m^2 = \sigma_{out}^2/(\sigma_{in} \cdot M)^2 = 2 \times (M-1)/M^{(N+1)/N} + 1/M$, where M is the total multiplication gain and N is the number of multiplication stages. In our case $N = 536$, $M \sim 100$ and consequently $F_m^2 \simeq 2$ and this increases Fano limited noise from 4.5e to 6.3e. The dark current shot noise is multiplied in the serial register but readout noise is not. Combining these noise sources, the resolution can be expressed as $\sigma_E/E = \sqrt{F_m^2(\sigma_{signal}^2 + K^2\sigma_{dark}^2) + K^2(\sigma_{read}/M)^2}/N_e$, where K is the x-ray cluster size, 5 in this analysis. Other contributions into the total output signal variance, such as deferred charge noise when there is trapping and photon beam energy spread should be taken into considerations as well.

The energy resolution was measured as the width of the x-ray peak shown in the right plot in Fig.1 and presented in Table 2 for both #0 and #1 sensors at the SIX beam line. The peak position was used to calculate the conversion coefficient $C = E[eV]/A_{peak}[adu]$. In terms of multiplication and electronics, G, gains $A_{peak} = M \cdot G \cdot N_e$ and $C = w/MG$. Converting the read noise from a.d.u to eV this way produces easy to interpret quantity $\sigma_{conv} = C \cdot G \cdot \sigma_{read} = w \cdot \sigma_{read}/M$, where σ_{read} is the equivalent noise charge on the electronics input. The resulting σ_{read} at different temperatures are summarized in Table 2. Both sensors behave very similar and readout noise values in Table 2 are presented for sensor #0. The total noise r.m.s. derived from the energy resolution is $\sim 18e$. The main contribution is from the readout noise and generally the total noise behaves according to expectations. For example, the effective readout noise increases when the multiplication gain decreases at warmer temperatures. The latter effect however can be compensated by a small increase in the HV phase amplitude. It should be noted that the pixel noise amplitude distribution is non-Gaussian with a tail towards larger amplitudes. This indicates that dark current noise contribution,

Table 2: Noise and energy resolution summary.

T, C	σ_{read}, adu	Scale, eV/adu	K σ_{read}/M, e	σ_E/E, % (0)	σ_E/E,% (1)
-110	6.1	0.99	8.1	12.9	13.1
-105	5.86	1.15	9.1	12.8	12.7
-100	5.67	1.35	10.3	13.5	13.2
-95	5.53	1.6	11.9	14.0	13.3

light pollution, clock induced charge and some degree of correlations in the readout noise could be present. Further studies are required for clarification.

CONCLUSIONS

It was demonstrated that the x-ray average cluster shape and cluster correlation matrix analysis can reveal charge distribution asymmetries. This analysis provides practical and robust measurements with a good accuracy for modest, $\sim 20k$ statistical samples. This tool enables us to perform sensor performance optimization. At nominal operating conditions both average cluster shape and correlation matrix were non-symmetrical with a "tail" behind the central pixel, in serial direction. The temperature adjustment from -110C to -95C restored the symmetry. Correlation coefficients all become negative, as expected, with values down to -0.12. The multiplication gain temperature dependence was observed. The gain decreases with rising temperature, as expected.

It is demonstrated that x-ray analysis is a powerful tool for EMCCD characterization and performance optimization.

ACKNOWLEDGMENTS

Authors acknowledge XCAM x-ray detector development efforts. This manuscript has been co-authored by employees of Brookhaven Science Associates, LLC. This research used beam line 2-ID of the National Synchrotron Light Source II, a U.S. Department of Energy (DOE) Office of Science User Facility operated for the DOE Office of Science by Brookhaven National Laboratory under Contract No. DE-SC0012704.

References

[1] I.Jarrige, V.Bisogni, Y.Zhu, W.Leonhardt, and J.Dvorak, "Paving the way to ultra-high-resolution resonant inelastic x-ray scattering with the six beamline at nsls-ii," *Synch. Rad. News* **31**(2), pp. 7–13, 2018.

[2] XCAM, "Rixscam - a multi-emccd large detector area system."

[3] E.D.Palik, ed., *Handbook of Optical Constants of Solids*, Academic Press, New York, 1985.

[4] T.E.Everhart and P.H.Hoff, "Determination of kilovolt electron energy dissipation vs penertation distance in solid materials," *J.Appl.Phys.* **42**, p. 5837, 1971.

[5] J.R.Janesick, *Scientific charge-coupled devices*, vol. xvi of *SPIE Press.*, Bellingham, Wash., 2001.

[6] G.G.Pavlov and J.A.Nousek, "Charge diffusion in ccd x-ray detectors," *Nuclear Inst. and Methods in Physics Research* **A428**, pp. 348–366, 1999.

[7] A. Amorese and et. al., "Enhanced spatial resolution of commercial soft x-ray ccd detectors by single-photon centroid reconstruction," *Nuclear Instruments and Methods in Physics Research Section A* **A935**, pp. 222–226, 2019.

[8] I.V.Kotov, J.Haupt, P.Kubanek, P.O'Connor, and P.Takacs, "X-ray analysis of fully depleted ccds with small pixel size," *Nuclear Instruments and Methods in Physics Research Section A* **787**, pp. 12–19, 2015.

[9] K. Pearson, "Contributions to the mathematical theory of evolution," *Psychological transactions of the Royal Society of London* **A, 186**, pp. 343–414, 1895.

[10] N. Bush, K. Stefanov, D. Hall, D. Jordan, and A. Holland, "Simulations of charge transfer in electron multiplying charge coupled devices," *Journal of Instrumentation* **9(12)**, p. C12042, 2014.

[11] e2v Technologies, "CCD207-40 datasheet," 2016.

[12] G.W.Frase and et al., "The X-ray energy response of silicon. part A. theory," *Nuclear Instruments and Methods in Physics Research* **A350**, pp. 368–378, 1994.

[13] M.S.Robins and B.J.Hadwen, "The noise performance of electron multiplying charge-coupled devices," *IEEE Trans. Electron Devices* **50**, pp. 1227–1232, May 2003.